Small Methods

small methods
www.small-methods.com

RESEARCH ARTICLE

Continuous Synthesis of Optimized $Ni_3(HITP)_2$ With Broad Spectrum of Morphologies via Automated Microfluidic Ammonia Manipulation Platform

Jingyang Zhao[1,2] | Chao Liang[2] | Jiajun Li[2] | Yi Huang[2] | Chaoqun Niu[2,3] | Hanqing Jiang[2,3]

[1]School of Materials Science and Engineering, Zhejiang University, Hangzhou, Zhejiang, China | [2]School of Engineering, Westlake University, Hangzhou, Zhejiang, China | [3]Westlake Institute for Advanced Study, Hangzhou, Zhejiang, China

Correspondence: Chao Liang (liangchao@westlake.edu.cn) | Hanqing Jiang (hanqing.jiang@westlake.edu.cn)

Received: 12 February 2026 | **Revised:** 1 May 2026 | **Accepted:** 20 May 2026

Keywords: ammonia borane | hydrogen generation | metal-organic framework | microfluidics | morphology manipulation

ABSTRACT

The morphology of metal–organic frameworks (MOFs) critically governs their electronic, catalytic, and transport performance. However, continuous synthesis of morphology-tunable MOFs remains challenging because scaffold formation is influenced by and highly sensitive to subtle reaction condition variations, involving temperature, concentration, mixing rate, and pH. Here, we present a programmable reactor for iterative synthesis of MOFs via Microfluidics (PRISMM) that enables precise and continuous synthesis of $Ni_3(HITP)_2$ and Pt-decorated $Ni_3(HITP)_2$ with a broad spectrum of morphologies, ranging from disordered aggregates to well-defined nanosheets, thereby allowing a wide distribution of porosity. By independently regulating ammonia permeation through microfluidic chips and dynamically adjusting synthesis parameters, this platform achieves fine control over ligand deprotonation kinetics and nucleation in a continuous and reproducible manner. The resulting $Ni_3(HITP)_2$ exhibits optimized morphology and enhanced porosity, while incorporation of platinum maximizes Pt accessibility and exposure, facilitates rapid mass transfer, and improves active-site utilization. In ammonia borane dehydrogenation, $Pt@Ni_3(HITP)_2$ delivers 3 equivalents of hydrogen with over 99% purity, yielding a turnover frequency of 2323 min^{-1}. This work establishes an automated pathway for MOF morphology manipulation, thereby demonstrating the strong potential of programmable microfluidic synthesis for morphology-directed design of MOFs in energy, catalytic, and broader applications.

1 | Introduction

Metal-organic frameworks (MOFs) are a class of crystalline porous materials constructed from metal nodes connected by organic ligands [1, 2]. Due to their exceptionally high surface area (up to ≈7000 m^2 g^{-1}) [3], tunable pore sizes (from below 2 nm to over 50 nm) [4], and versatile surface chemistry that allows modification [5] and functionalization [6], MOFs have been explored for diverse applications, ranging from clean energy storage and conversion [7, 8], water treatment [9], drug delivery [10], and chemical sensing [11], among many others [12–18]. In these applications, both the chemical composition and morphology of MOFs are critical, since morphology governs the way these intrinsic properties are expressed [19]. For example, how accessible the surface is or how efficiently molecules can diffuse through pores. These critical structural features, however, are highly sensitive to synthesis conditions. Even slight variations in parameters, such as temperature [20, 21], precursor concentration [22], solvent polarity [23], or pH [24] can drastically alter the balance between nucleation and growth, leading to different morphologies.

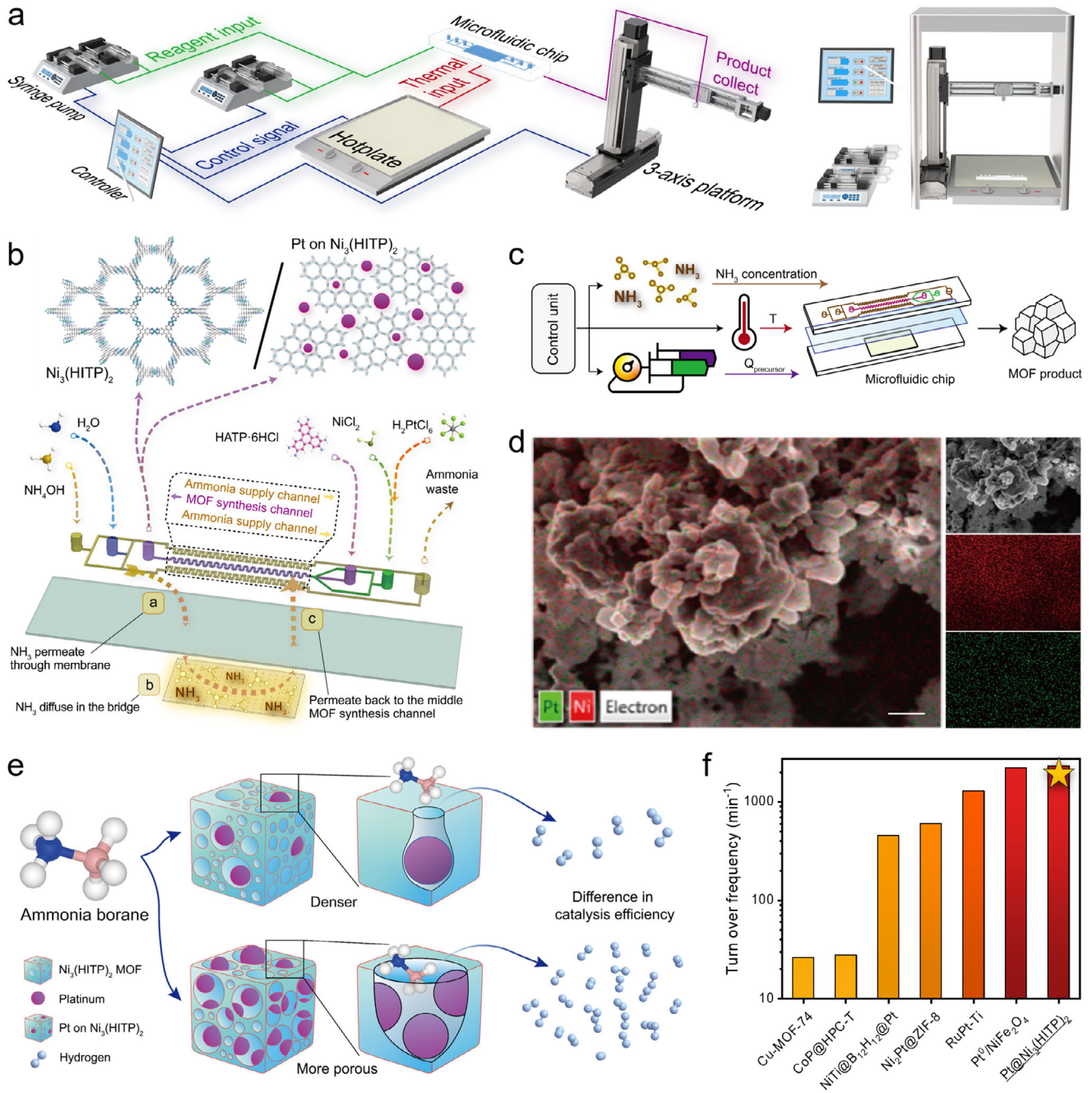

FIGURE 1 | Design and working principle of the PRISMM platform for programmable MOF synthesis and catalysis. (a) Exploded and assembled view of PRISMM. (b) Schematic of double ammonia permeation through a thin membrane and dissolving into the MOF synthesis channel. (c) Schematic of parameter control during MOF synthesis. (d) SEM and EDS overlay image of Pt@$Ni_3(HITP)_2$. Scale bar: 500 nm. (e) Schematic of Pt@$Ni_3(HITP)_2$ exhibiting superior catalytic performance in ammonia borane (AB) dehydrogenation. (f) TOF comparison of different Pt/MOF related catalysts.

Conventional batch synthesis methods lack precise control over both morphologies and the key synthesis parameters, constraining the applications of the scaffold. For instance, the ammonia vapor diffusion method can roughly adjust the amount of ammonia additive to facilitate low-temperature synthesis [25], but the resulting control remains limited. Besides these strategies [26–30], microfluidic methods have drawn particular attention because their small channel dimensions maintain laminar, predictable flow and enable more efficient heat and mass transfer than bulk reactors [31]. These features create a more uniform reaction environment that improves reproducibility in MOFs synthesis [32]. For example, a microfluidic solution-shearing method was used to produce flexible, transparent ultrathin MOF membranes, demonstrating the capability of microfluidic systems for framework synthesis [13, 33]. Nevertheless, current microfluidic platforms still face significant limitations: most designs cannot precisely control chemical concentration along the synthesis channel [32, 34], and many studies only control a single synthesis parameter rather than multiple variables [33–35].

To address these limitations, we developed a new microfluidic platform, programmable reactor for iterative synthesis of MOFs

via microfluidics (PRISMM), to produce scalable morphologies. This system enables the simultaneous control of multiple synthesis parameters, including temperature, ammonia concentration, and precursor ratio, within a single, continuous process. The platform is built around a multilayer microfluidic chip (Figure 1a), where a dedicated synthesis channel is coupled to ammonium hydroxide (NH_4OH) supply channels through an intermediate bridge chamber (Figure 1b). With this setup, one can systematically study how different synthesis conditions affect MOF morphology (Figure 1c). As a model system, $Ni_3(HITP)_2$, is chosen for two main reasons. First, as a 2D conductive MOF [36], $Ni_3(HITP)_2$ has been widely investigated for sensing [11], electrocatalysis [12, 37], and energy-related [8] applications. Second, its performance in these areas is strongly influenced by its morphology, yet reliable methods to control morphology with multiparameter, especially ammonia additive, have been lacking [38]. To further demonstrate the capability of PRISMM, we decorated $Ni_3(HITP)_2$ with platinum (Pt) (Figure 1d) and evaluated its catalytic performance for hydrogen release from ammonia borane (AB), a solid hydrogen carrier with high H_2 density (Figure 1e). The Pt@$Ni_3(HITP)_2$ catalysts synthesized using PRISMM show optimized porosity, and effective Pt incorporation, leading to enhanced catalytic activity within the PRISMM-derived sample series. Under the tested conditions, the optimized catalyst achieves a TOF of 2,323 min^{-1}, placing it among highly competitive reported Pt-based catalysts for ammonia borane dehydrogenation while the literature comparison is intended as general performance context (Figure 1f) [39–44]. These results demonstrate that PRISMM serves not only as a platform for systematic morphology–property studies, but also as a practical tool for producing high-performance MOF-based catalysts.

2 | Results and Discussion

2.1 | Programmable Microfluidic Platform for Automated Synthesis

The PRISMM platform enables automated and precise environmental control for MOF synthesis under continuously tunable conditions. The platform integrates a multilayer microfluidic chip, multichannel syringe pumps for reagent delivery, a programmable hotplate for temperature management, and a three-axis robotic stage for positioning and sample handling (Figure 1a and Figure S1). All components are connected through a central controller to coordinate motion, reagent flow and thermal supply with pre-set programs.

The core of the system is the multilayer PDMS–glass microfluidic chip (Figure 2a and Figure S2), which implements dual ammonia permeation to regulate the reaction environment. An ammonia-permeable membrane separates the lower NH_3 bridge layer from the upper synthesis layer, where MOF formation occurs. The synthesis layer contains inlets for Ni^{2+} and HITP solutions and a single outlet for collecting the $Ni_3(HITP)_2$ product (Figure 2b and Figure S3). During operation, the precursor solutions are continuously injected by syringe pumps and mixed within the serpentine synthesis channel. As the reaction proceeds, HITP linkers deprotonate and coordinate with Ni^{2+} ions to form $Ni_3(HITP)_2$ nuclei (Figure S4), which then grow into larger particles carried along by the flow. However, as nucleation continues, larger particles tend to settle in regions of low fluid velocity, particularly at sharp corners of the serpentine channel, where they accumulate and eventually clog the channel (Figure S5). Filleting the channel corners to remove low-velocity 'dead zones' yielded an optimized flow channel with a more uniform flow field and long-term continuous operation without precipitation or clogging (Figure S6 and Video S1).

The ammonia supply channels occupy the outer regions of the top layer and continuously deliver ammonia vapor around the MOF synthesis channel (Figure 2c, left). In the nucleation and MOF growth, ammonia functions as a base to deprotonate the HITP ligands, promoting metal-ligand coordination to form the Ni-HITP framework (Figure S4). The delivery of ammonia is governed by a two-step permeation mechanism across the PDMS membrane: first, ammonia diffuses from the flowing NH_4OH solution into the intermediate gas bridge layer, and second, it permeates upward through the PDMS membrane into the synthesis channel (Figure 2c, middle and right). This dual diffusion path is designed to buffer concentration gradients and maintain a uniform ammonia distribution along the reaction channel. Qualitative pH-indicator imaging (Figure S7 and Video S2), numerical simulations (Figure S8), and a Nessler-based colorimetric calibration (Figure S9) of outlet samples validate this dual-permeation mechanism and quantify dissolved ammonia as NH_4^+ in the synthesis channel.

Using this calibrated platform, the regulation experiments were performed to control the dissolved NH_3 levels in the synthesis channels. At a constant temperature of 55°C, a thinner PDMS membrane and a higher ammonia supply concentration both lead to higher ammonia levels in the synthesis channel, mainly due to lower diffusion resistance and a stronger concentration gradient from the source (Figure 2d). Conversely, when the membrane thickness is fixed at 300 μm, increasing either the temperature or the NH_4OH solution concentration in the supply channels raises the ammonia level in the synthesis channel (Figure 2e). We then performed short- and long-term equilibrium tests using the same setup. The response test shows that, after a programmed change in the ammonia supply, the NH_3 concentration in the synthesis channel stabilizes within 45–60 s, indicating sufficiently fast regulation for continuous synthesis (Figure S10). Long-term stability tests show minimal drift over 10 h of continuous operation, confirming that both the microfluidic chip and the dual ammonia permeation design remain stable during extended runs (Figure 2f, Video S3 shows a 2-hour visualization with the indicator). To further evaluate the compatibility of the PDMS membrane with continuous ammonium hydroxide exposure, we characterized the membrane after different exposure durations. FTIR spectra showed no obvious changes in the characteristic vibration regions, and membrane thickness measurements showed no detectable swelling within experimental uncertainty (Figure S11). Together with the stable ammonia concentration observed during the 10 h operation test (Figure 2f), these results indicate that PDMS swelling and the associated drift in ammonia diffusion are negligible under the present operating conditions.

The dissolved NH_3 concentration is regulated by both the syringe pumps and the temperature, while temperature itself serves as an independent parameter during MOF synthesis. Temperature control is achieved using a programmable hotplate mounted

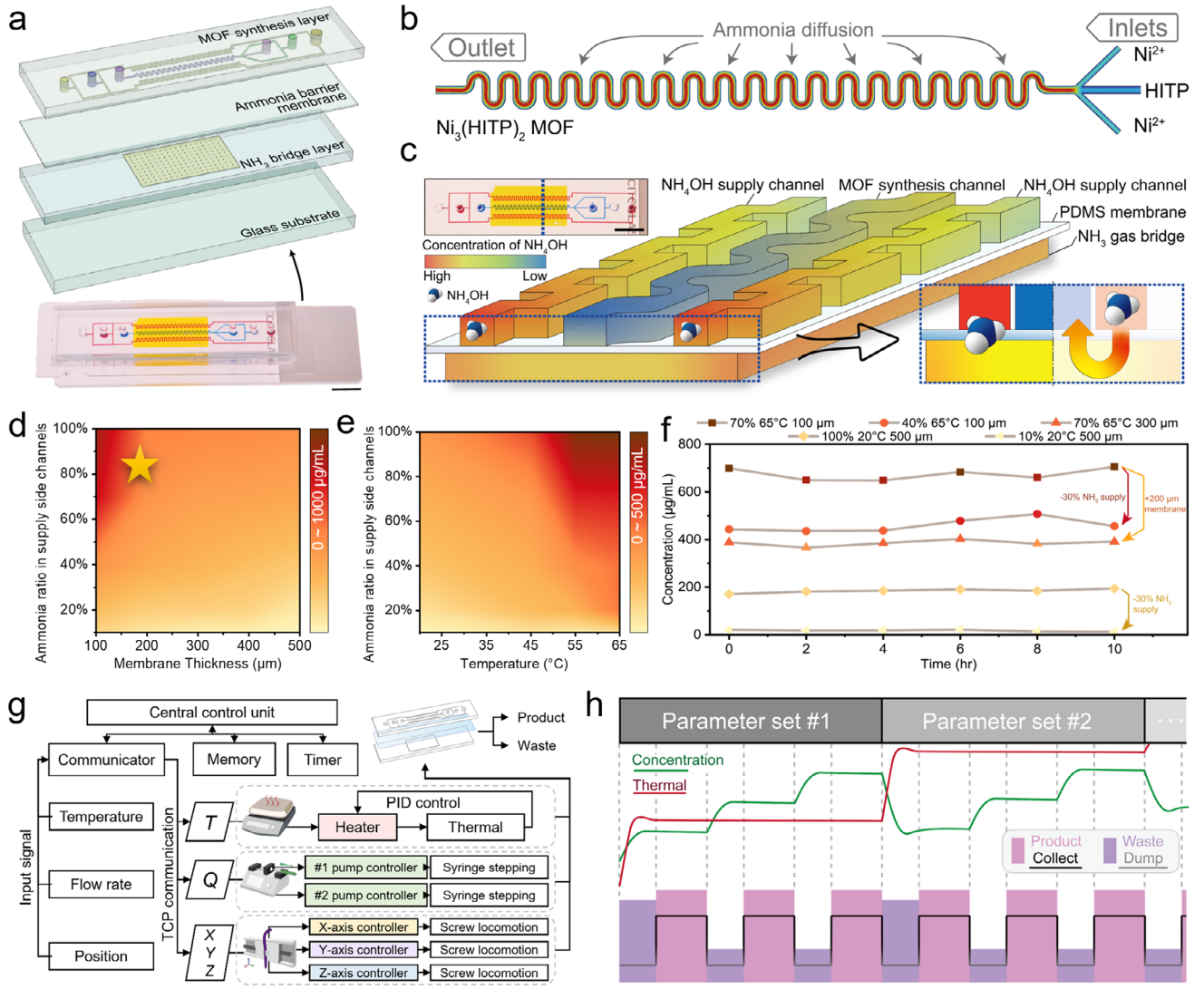

FIGURE 2 | Microfluidic architecture and ammonia transport characteristics of the PRISMM chip. (a) Photograph of the PRISMM chip and exploded view of multilayer structure. Scale bar: 10 mm. (b) Simulation of flow velocity profile of the synthesis channel. (c) Top view (left top), oblique projection (middle), slice view (right) of the dual permeation process (In slice view: red: NH_4OH channel; blue: MOF synthesis channel; yellow: NH_3 bridge; light blue: PDMS membrane). (d) Heatmap of equivalent NH_4^+ concentration in MOF synthesis channel with different ammonia supply and membrane thickness at fixed temperature 55°C (scale from 0 to 1000 μg mL^{-1}). (e) Heatmap of equivalent NH_4^+ concentration in MOF synthesis channel with different ammonia supply and temperature conditions and fixed membrane thickness 300 μm (scale from 0 – 500 μg mL^{-1}). (f) Long-term stability of equivalent NH_4^+ concentration in synthesis channel. (g) Diagram of control signal that facilitates the iterative synthesis. (h) Schematic of the strategy in sample collection and dump.

beneath the microfluidic chip that applies multistep heating profiles from room temperature to 65°C with stable setpoints (Figure S12), thereby ensuring precise and consistent thermal conditions throughout synthesis cycles. With both NH_3 concentration and temperature regulated, the microfluidic chip can continuously produce MOF materials under programmed conditions. To separate products collected under different synthesis parameters, a three-axis stage equipped with independent motors and a control board (Figure S13) provides spatial precision for sample handling (Figure S14 and Video S4).

All synthesis steps, from NH_3 and temperature regulation to product collection, are executed automatically following predefined scripts. The control program coordinates the different modules, adjusting thermal input, pump rates, and stage motion (Figure 2g), forming a fully functional programmable reactor for iterative MOF synthesis. MOF suspensions produced under various conditions are collected or discarded following a logical sequence: once the synthesis reaches a steady state, the stage moves to the collection position; during parameter transitions (temperature or dissolved NH_3 change), the arm redirects to the waste container to discharge transitional products, then returns for the next stable collection (Figure 2h and Video S4).

Altogether, this system establishes a programmable microfluidic platform that integrates chemical, temperature, and flow regulation. It enables continuous and morphology-controlled synthesis of $Ni_3(HITP)_2$ and its derivatives, providing a versatile foundation for high-throughput catalyst optimization and automated reactions.

2.2 | Porosity and Morphology Manipulation of $Ni_3(HITP)_2$ MOF Using PRISMM

Dissolved ammonia plays an essential role in the synthesis of $Ni_3(HITP)_2$, serving as both a base and a diffusive modulator. In the synthesis channel, OH^- abstracts protons from the —NH groups of HITP, creating active sites for Ni^{2+} coordination. Ni^{2+} ions undergo ligand exchange with NH_3 and progressively link with the deprotonated nitrogen sites, reducing their hydration shells and anchoring into a planar structure that nucleates the 2D $Ni_3(HITP)_2$ framework (Figure S4). This mechanism highlights the importance of NH_3 as a chemical additive and temperature as a kinetic driver in the synthesis process.

To study how protonation and thermal input affect the formation of $Ni_3(HITP)_2$, we prepared samples under different NH_3 concentrations and temperatures using the PRISMM platform (starting conditions shown in Figure 2f). The resulting materials displayed distinct morphologies (Figure 3a):

1. At low to medium ammonia concentration (100 and 500 μg mL^{-1}) and low temperature (35°C), incomplete ligand deprotonation limits coordination and slows nucleation, producing plate-like morphologies (Figure 3a, orange frame; Figure S15a). Under these conditions, nucleation processes are sparse and crystal growth proceeds in a diffusion-limited regime. This biases growth toward lateral extension rather than vertical stacking, resulting in large, smooth platelets.
2. As ammonia concentration or temperature increases, deprotonation and coordination become faster, leading to denser nucleation and mixed reticulate or branched assemblies (Figure 3a, red frame). Higher NH_3 concentration increases the supply of OH— and accelerates deprotonation, leading to a high density of reactive linker sites and denser nucleation as well. Multiple nuclei grow simultaneously and compete for precursor supply, yielding reticulate or branched domains composed of fused crystallites of different shapes (Figure 3a red frame). Even under moderate thermal input (35°C), elevated NH_3 sustains rapid deprotonation, giving rise to radially stacked rod assemblies (Figure 3a3). In contrast, insufficient NH_3 in moderate to high temperature range (45–65°C) leads to partially deprotonated ligands and uneven coordination, thus showing anisotropic stacking of clustered plates (Figure 3a4) and lamellar-flakes (Figure 3a7,10 and Figure S15b). In the regime of moderate temperature (45–55°C) and medium to high NH_3 (500–800 μg mL^{-1}), coordination is synchronized with deprotonation, resulting in controlled competitive growth that produces granular clusters (Figure 3a5,6) and a hierarchically porous framework (Figure 3a8).
3. When both ammonia concentration and temperature are relatively high (800 μg mL^{-1} at 55–65°C, and 500 μg mL^{-1} at 55°C), more rapid deprotonation and growth produce porous nanorod and nanosheet assemblies with more open interparticle voids (Figure 3a, purple frame; Figure S15b). In this high-flux regime, nucleation and growth occur rapidly yet coherently, producing thin, highly crystalline 2D sheets and bundles. These nanosheets readily undergo lateral fusion and π–π stacking, forming continuous reticulate porous network assemblies with well-defined edges. These results reveal a coherent pathway for morphology evolution governed by the coupled ammonia–temperature conditions, balanced among linker deprotonation kinetics, Ni^{2+} coordination rate, and interlayer diffusion.

The PXRD patterns of the PRISMM samples exhibit the characteristic reflections of $Ni_3(HITP)_2$ and agree well with the reference pattern, confirming successful framework formation (Figure 3b). A vapor-diffusion sample was also measured as a bulk reference (Figure S16). The close agreement in peak positions between the PRISMM and vapor-diffusion samples indicates that both methods produce the same $Ni_3(HITP)_2$ crystalline phase. Compared with the vapor-diffusion sample, the PRISMM samples exhibit broader and weaker reflections, suggesting reduced long-range crystallinity and smaller crystallite domains associated with their nanoscale morphologies. To further confirm the formation of $Ni_3(HITP)_2$ and evaluate residual precursor species, FTIR and XPS analyses were performed (Figure S17). The XPS survey spectrum shows the expected Ni, N, and C signals, and the high-resolution Ni 2p spectrum displays characteristic Ni 2p peaks with satellite features, consistent with Ni in a coordinated ionic environment. FTIR further shows the characteristic vibrations of the coordinated HITP skeleton, including C═N/C—N related bands in the 1600–1000 cm^{-1} region. No obvious residual peaks associated with free HITP or uncoordinated precursor species are observed, suggesting effective framework formation and negligible trapped precursors after washing.

We then characterized the porosity of these samples using nitrogen adsorption–desorption isotherms. Because N_2 adsorption in $Ni_3(HITP)_2$ can be kinetically slow at 77 K, the adsorption measurements were repeated with longer equilibration times at each relative pressure to ensure sufficient pore filling. The relative pressure-adsorbed volume curves (Figure 3c) show that samples synthesized under higher NH_3 and temperature display steeper adsorption/desorption branches, indicating enhanced microporosity and more accessible pore openings. Conversely, lower NH_3 and temperature produce flatter curves, consistent with incomplete framework formation. BET analysis (Figure 3d) further supports this trend: samples from high-NH_3 and high-temperature synthesis exhibit smaller slopes in the linearized plots, corresponding to larger surface areas. Notably, samples enriched in nanosheet or nanorod assemblies show not only higher BET surface areas but also faster adsorption kinetics and larger hysteresis loops (Figure 3c gray loop), consistent with improved framework crystallinity and increased inter-sheet voids. These observations demonstrate that the ammonia-temperature synthesis window governs not only the intrinsic MOF pore structure but also the hierarchical mesoporosity generated from morphology-dependent particle packing. Pore-size distributions obtained from BJH analysis (Figure 3e) reveal that samples synthesized under strong ammonia and thermal conditions possess a broad mesopore range (5–100 nm), while those from low-NH_3-temperature conditions show narrower, flatter distributions. This widening of mesopore size reflects the emergence of inter-sheet voids and defect-mediated cavities (Figure 3a11,12 and Figure S15c) formed during high nucleation and growth regimes. In contrast, low ammonia-temperature synthesis produces tightly packed platelets with limited interparticle spacing, resulting in only subtle mesopores (Figure 3a1–4). The richer mesoporous structure facilitates better mass transfer in nanoscale

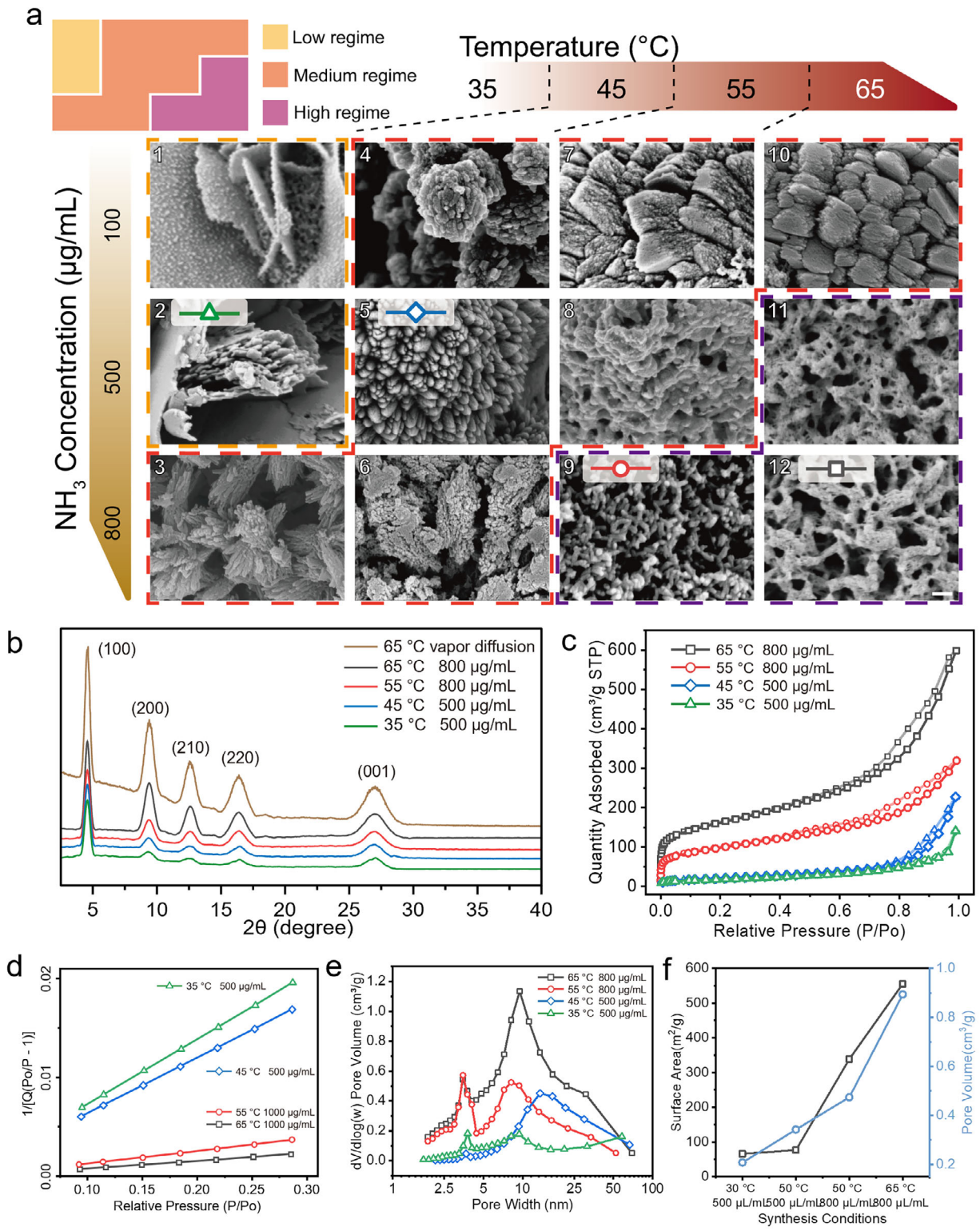

FIGURE 3 | Structural and porosity evolution of $Ni_3(HITP)_2$ under programmable synthesis conditions. (a) SEM image matrix of $Ni_3(HITP)_2$ synthesized at different temperatures and ammonia concentrations. The columns correspond to synthesis temperatures of 35, 45, 55, and 65°C, and the rows correspond to ammonia concentrations of 100, 500, and 800 μg mL^{-1}. Colored outlines indicate representative morphology regimes observed across the synthesis window; the same symbols are used in panels (c–f) to link each porosity measurement to its corresponding synthesis condition and SEM morphology. Scale bar: 100 nm. (b) PXRD patterns of representative $Ni_3(HITP)_2$ samples, showing characteristic reflections of $Ni_3(HITP)_2$ and condition-dependent changes in peak intensity and width. (c) N_2 adsorption–desorption isotherms of representative $Ni_3(HITP)_2$ samples. (d) BET linear fitting plots derived from the N_2 adsorption isotherms. (e) Pore-size distribution curves calculated from the desorption branch, showing the condition-dependent development of mesopores. (f) Summary of BET specific surface area and total pore volume, showing increased accessible porosity under high-ammonia and high-temperature synthesis conditions.

flow environments (Figure 3a11,12). BET analysis (Figure 3f) further supports this trend, with surface areas increasing from 65.68 to 555.47 $m^2\ g^{-1}$ across the investigated synthesis conditions. The corresponding total pore volumes also increase from 0.21 to 0.89 $cm^3\ g^{-1}$, confirming that optimized PRISMM conditions substantially improve porosity relative to low-ammonia and low-temperature synthesis. Although the highest BET surface area remains lower than some literature values for highly crystalline $Ni_3(HITP)_2$, the present result demonstrates that PRISMM can tune accessible porosity and morphology-derived mesoporosity through programmed ammonia and temperature control [38].

To evaluate reproducibility, independent PRISMM syntheses were repeated under representative ammonia concentration and temperature conditions. The repeated samples showed comparable yields, BET surface areas, and pore-size distributions, confirming that the programmed ammonia and temperature conditions can be reproduced in independent synthesis runs (Table S1). To benchmark PRISMM against a conventional ammonia vapor diffusion method, $Ni_3(HITP)_2$ samples were prepared under comparable precursor concentrations and compared in terms of yield, productivity, surface area, and pore-size distribution (Table S1 and Figure S18). Both methods gave comparable product yields. The current single-channel PRISMM device showed lower productivity than batch vapor diffusion because of the limited microfluidic channel capacity. However, PRISMM enabled programmable regulation of ammonia concentration and temperature during continuous synthesis, resulting in a broader range of accessible morphologies and substantially higher surface areas under optimized conditions. In particular, optimized PRISMM samples exhibited pronounced mesopore distributions, whereas vapor-diffusion samples showed relatively narrow pore distributions and lower surface areas. Specifically, the surface area of PRISMM samples ranged from approximately 64 to 555 $m^2\ g^{-1}$, whereas vapor-diffusion samples were limited to approximately 96 to 122 $m^2\ g^{-1}$ under the tested conditions (Table S1). These results indicate that the primary advantage of PRISMM lies in programmable morphology and porosity control rather than maximum mass productivity in the current device configuration. Under the optimized condition, the current single-channel PRISMM device produced $Ni_3(HITP)_2$ at a rate of approximately 55.9 mg h^{-1}, corresponding to 1341.6 mg per day under uninterrupted operation. This throughput reflects the present laboratory-scale chip design and is limited by the channel volume and precursor flow rate; therefore, we describe the current platform as continuous and programmable rather than large-scale.

To evaluate whether the PRISMM synthesis conditions influence electronic transport, four-probe conductivity measurements were performed on representative $Ni_3(HITP)_2$ samples synthesized under different ammonia concentration and temperature conditions. All samples showed approximately linear *I–V* characteristics, indicating ohmic transport behavior (Figure S19). The calculated conductivities ranged from 63.88 to 84.62 S cm^{-1}, confirming that conductive $Ni_3(HITP)_2$ was obtained across different morphology regimes. No simple monotonic trend was observed between conductivity and either ammonia concentration or temperature. This is consistent with previous studies showing that charge transport in $Ni_3(HITP)_2$ is affected by multiple structural factors, including crystallinity, particle morphology, interparticle connectivity, packing density, and grain boundaries [45, 46]. Therefore, the present results support the formation of conductive $Ni_3(HITP)_2$, while a detailed conductivity–morphology correlation requires further systematic study.

Beyond these two essential factors, the PRISMM strategy also provides a way to systematically explore other synthesis parameters such as solvent composition and linker-to-node ratio, by manipulating flow rate ratio of solvent and reagent input (Figure S20). In this way, the PRISMM potentially offers new insights into porosity control in MOFs.

2.3 | High Efficiency Hydrogen Release From Ammonia Borane Catalyzed by Pt@$Ni_3(HITP)_2$

To evaluate the performance of the optimized $Ni_3(HITP)_2$, we decorated the framework with platinum to catalyze the dehydrogenation of ammonia borane (NH_3BH_3, AB). AB is a solid hydrogen carrier with high hydrogen density and can release up to three equivalents of H_2 per mole. The dehydrogenation reaction proceeds at room temperature through cleavage of B—H and N—H bonds, where the Pt@$Ni_3(HITP)_2$ catalyst provides abundant active sites that lower the activation barrier and accelerate H—H formation (Figure 4a). In this system, the $Ni_3(HITP)_2$ framework serves as a porous support, while the deposited Pt enhances electron transfer and adsorption–desorption kinetics, together leading to enhanced catalytic activity. [Correction added on June 11, 2026, after first online publication: A typo error in Chemical bond has been corrected in this version.]

The Pt@$Ni_3(HITP)_2$ catalysts were synthesized on the PRISMM platform under different combined conditions of ammonia concentrations and thermal conditions, tuning their morphology and porosity to improve hydrogen release. SEM images confirm clear structural differences among the samples prepared under different conditions (Figure 4b). These structural differences directly influence catalytic performance. Hydrogen evolution experiments show that the catalysts produced under higher ammonia concentration and temperature exhibit faster H_2 release rates (Figure 4c). The stability of the catalyst was further evaluated through repeated hydrogen release cycles using the same sample. It is found that the total amount of released hydrogen remained nearly constant across cycles, indicating good reusability (Figure 4d).

To better understand the catalytic efficiency, temperature-programmed desorption (TPD) was used to quantify the density of catalytically accessible Pt sites (Figure S21). Samples synthesized under coupled high ammonia and temperature conditions showed the highest active-site density (0.17 mmol g^{-1}), increasing from 0.07 to 0.10, 0.11, and finally 0.17 mmol g^{-1}, consistent with their hydrogen evolution performance (Figure 4e). The corresponding turnover frequency (TOF) increased from 507 to 1426, 1842, and up to 2323 mol H_2 $mol_{accessible\ Pt\ sites}^{-1}$ min^{-1} for the sample with the densest active sites and largest surface area and pore volume, demonstrating the advantage of controlled synthesis using PRISMM. Because reported TOF values for ammonia borane dehydrogenation are often obtained under different catalyst loading, Pt loading, AB concentration, temperature, solvent, and calculation protocols, the comparison in Figure 1f is intended

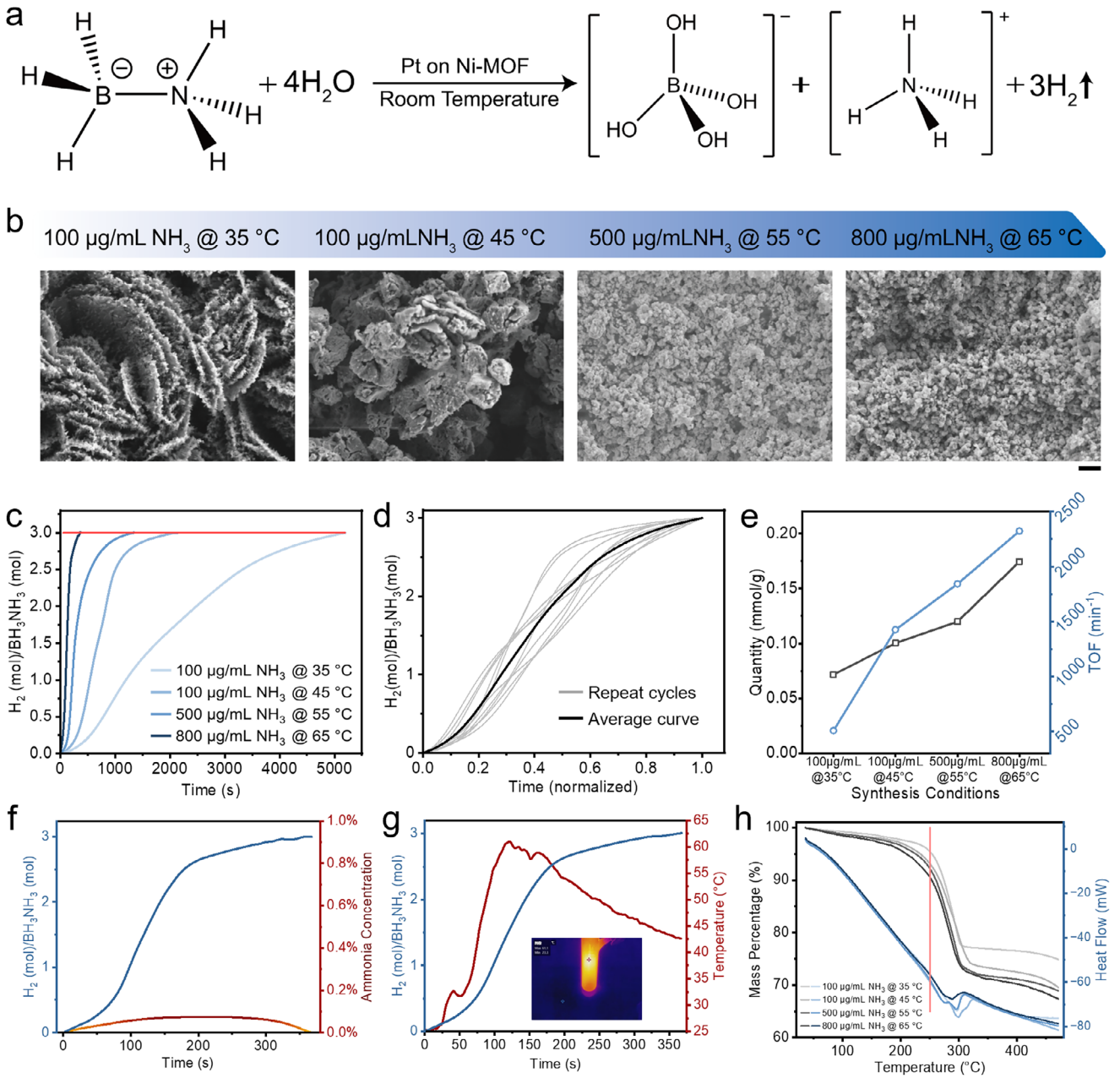

FIGURE 4 | Catalytic performance and thermal stability of Pt@Ni_3(HITP)$_2$ for ammonia borane dehydrogenation. (a) Schematic illustration of hydrolytic dehydrogenation of ammonia borane (AB) catalyzed by Pt@Ni_3(HITP)$_2$ in water at room temperature, releasing up to three equivalents of H_2. (b) SEM images of Pt@Ni_3(HITP)$_2$ prepared under representative PRISMM synthesis conditions, showing morphology evolution from platelet-like structures to porous nanostructures. Scale bar: 500 nm. (c) Time-dependent H_2 evolution during AB dehydrogenation catalyzed by Pt@Ni_3(HITP)$_2$ samples synthesized under different conditions. The H_2 amount is plotted as the molar equivalent of H_2 released per mole of AB. (d) Time-normalized H_2 evolution profiles from repeated catalytic runs using the same Pt@Ni_3(HITP)$_2$ catalyst. Individual cycles are shown in gray, and the averaged profile is shown in black, demonstrating reproducible catalytic behavior. (e) Comparison of catalytically accessible Pt-site density and corresponding turnover frequency (TOF) for Pt@Ni_3(HITP)$_2$ samples prepared under different conditions. (f) Simultaneous monitoring of H_2 evolution and NH_3 byproduct concentration during AB dehydrogenation, showing limited ammonia release during the reaction. (g) Time-dependent H_2 evolution and reaction-temperature profile during AB dehydrogenation. Inset: infrared thermal image recorded near the highest reaction temperature. (h) Simultaneous TGA–DSC profiles of Pt@Ni_3(HITP)$_2$ catalysts, showing mass change and heat flow during heating. The red vertical line marks the main thermal decomposition temperature region for the samples. (Unless otherwise stated, AB dehydrogenation tests were performed using 100 mg Pt@Ni_3(HITP)$_2$ catalyst and 10 wt% AB aqueous solution at room temperature. The Pt precursor concentration for catalyst preparation was 20 mM H_2PtCl_6, and the actual Pt/Ni ratios are provided in Figure S22. Catalytic traces represent single runs unless averages are explicitly indicated).

as a general performance context rather than a strict one-to-one benchmark. Under our test conditions, $Pt@Ni_3(HITP)_2$ synthesized under optimized PRISMM conditions exhibits a highly competitive TOF among reported Pt-based catalysts.

To better support the Pt-related catalytic analysis, we further characterized $Pt@Ni_3(HITP)_2$ samples by ICP-MS, XPS, and FTIR. ICP-MS quantified the actual Pt loading and Pt/Ni ratio in different samples, while XPS confirmed the presence of Pt together with Ni, N, and C in $Pt@Ni_3(HITP)_2$ (Figure S22). FTIR spectra indicate that the $Ni_3(HITP)_2$ framework is largely retained after Pt incorporation, with local changes in the chemical environment (Figure S23). The ICP-MS results show that samples with larger surface area and pore volume retain higher Pt/Ni ratios, suggesting that the porous framework provides more available sites and diffusion pathways for Pt incorporation. Together with the active-site-density measurements, these results support the correlation between PRISMM-controlled framework porosity, Pt incorporation, and catalytic performance.

In addition to activity, hydrogen purity is an important metric for ammonia borane dehydrogenation. Gas chromatography (GC) analysis confirmed that the released gas consisted almost entirely of hydrogen (Figure S24). In the fastest reaction, 95% of the stored hydrogen was released within 5 min, and only trace amounts of NH_3 byproduct were detected by an ammonia sensor (Figure 4f). When the catalyst loading was reduced, the NH_3 byproduct dropped below 20 ppm (0.002 vol%), as shown in Figure S25. The slight fluctuation in selectivity can be attributed to mild heat generation during dehydrogenation: in the rapid reaction test, the temperature rose to about 61°C from room temperature (Figure 4g). Lower catalyst loading reduced heat generation to less than a 2°C increase but extended the reaction time (Figure S26). Although the reaction heat is mild, thermal stability is a critical requirement for catalyst reliability. Thermogravimetric analysis (TGA) and differential scanning calorimetry (DSC) confirm that $Pt@Ni_3(HITP)_2$ remains stable up to 200°C with negligible mass loss and exhibits a nearly linear heat flow up to 250°C (Figure 4h), confirming its robustness under working conditions.

3 | Conclusions

PRISMM is a platform with multiparameter manipulation capability, making it a suitable system for next-generation MOF synthesis, regulation, and modification. By taking advantage of PRISMM, we achieved the synthesis of high-porosity $Ni_3(HITP)_2$ and its Pt-decorated derivatives via controlled experiments of multiparameters, especially dissolved ammonia concentration. The $Ni_3(HITP)_2$ materials synthesized using PRISMM span a wide range of porosity while remaining compatible with platinum incorporation. As a result, the $Pt@Ni_3(HITP)_2$ catalysts exhibit markedly improved ammonia borane dehydrogenation performance, with high efficiency and hydrogen purity. The improved catalytic activity can be attributed to two related factors: (1) the larger surface area and pore volume of the host framework, which favor Pt incorporation and provide more accessible diffusion pathways; and (2) the retained conductive $Ni_3(HITP)_2$ framework, which supports reactant transport and catalytic operation after Pt incorporation. PRISMM enables continuous, automated, and programmable MOF synthesis under controlled ammonia and temperature conditions. The current single-channel implementation defines a laboratory-scale platform for reproducible morphology and porosity control, while future increases in production throughput would require parallelized channel arrays or chip numbering-up.

Acknowledgements

We thank the Westlake Center for Micro/Nano Fabrication for facility support and technical assistance in fabricating the PRISMM chip, and the Instrumentation and Service Center for Physical Sciences and Molecular Sciences at Westlake University for help with sample measurement and data interpretation. We thank Westlake Education Foundation for supporting this work. The authors acknowledge funding support from the Natural Science Foundations of Hangzhou (Grant No. 2024SZRYBH180012).

Conflicts of Interest

The authors declare no conflicts of interest.

Data Availability Statement

The data that support the findings of this study are available from the corresponding author upon reasonable request.

References

1. H. Furukawa, K. E. Cordova, M. O'Keeffe, and O. M. Yaghi, "The Chemistry and Applications of Metal-Organic Frameworks," *Science* 341 (2013): 1230444, https://doi.org/10.1126/science.1230444.

2. L. Jiao, J. Y. R. Seow, W. S. Skinner, Z. U. Wang, and H.-L. Jiang, "Metal–organic Frameworks: Structures and Functional Applications," *Materials Today* 27 (2019): 43–68, https://doi.org/10.1016/j.mattod.2018.10.038.

3. O. K. Farha, I. Eryazici, N. C. Jeong, et al., "Metal–Organic Framework Materials with Ultrahigh Surface Areas: Is the Sky the Limit?," *Journal of the American Chemical Society* 134 (2012): 15016–15021, https://doi.org/10.1021/ja3055639.

4. W. Zhang, R. Taheri-Ledari, M. Saeidirad, et al., "Regulation of Porosity in MOFs: A Review on Tunable Scaffolds and Related Effects and Advances in Different Applications," *Journal of Environmental Chemical Engineering* 10 (2022): 108836, https://doi.org/10.1016/j.jece.2022.108836.

5. C. V. McGuire and R. S. Forgan, "The Surface Chemistry of Metal–organic Frameworks," *Chemical Communications* 51 (2015): 5199–5217, https://doi.org/10.1039/C4CC04458D.

6. X. Chen, S. M. Argandona, F. Melle, N. Rampal, and D. Fairen-Jimenez, "Advances in Surface Functionalization of Next-Generation Metal-Organic Frameworks for Biomedical Applications: Design, Strategies, and Prospects," *Chemistry* 10 (2024): 504–543, https://doi.org/10.1016/j.chempr.2023.09.016.

7. R. Wang, W. Yu, C. Sun, et al., "High-Hole-Mobility Metal–Organic Framework as Dopant-Free Hole Transport Layer for Perovskite Solar Cells," *Nanoscale Research Letters* 17 (2022): 6, https://doi.org/10.1186/s11671-021-03643-7.

8. T. Kim, S. Kang, S. Park, et al., "Radially Oriented $Ni_3(HITP)_2$ Microspheres as High-Performance Anode Materials for Li-Ion Capacitors with Exceptional Energy Density and Cycling Stability," *Journal of Power Sources* 603 (2024): 234449, https://doi.org/10.1016/j.jpowsour.2024.234449.

9. X. Liu, Y. Shan, S. Zhang, Q. Kong, and H. Pang, "Application of Metal Organic Framework in Wastewater Treatment," *Green Energy & Environment* 8 (2023): 698–721, https://doi.org/10.1016/j.gee.2022.03.005.

10. S. He, L. Wu, X. Li, et al., "Metal-Organic Frameworks for Advanced Drug Delivery," *Acta Pharmaceutica Sinica B* 11 (2021): 2362–2395, https://doi.org/10.1016/j.apsb.2021.03.019.

11. W. Dai, K. Wen, X. Meng, S. Yu, J. Zhao, and Q. Lin, "Aptameric Metal–Organic Framework Nanobiosensor," *ACS Applied Nano Materials* 7 (2024): 17081–17091.

12. E. M. Miner, T. Fukushima, D. Sheberla, L. Sun, Y. Surendranath, and M. Dincă, "Electrochemical Oxygen Reduction Catalysed by Ni_3(hexaiminotriphenylene)2," *Nature Communications* 7 (2016): 10942, https://doi.org/10.1038/ncomms10942.

13. J.-O. Kim, W.-T. Koo, H. Kim, et al., "Large-Area Synthesis of Nanoscopic Catalyst-Decorated Conductive MOF Film Using Microfluidic-Based Solution Shearing," *Nature Communications* 12 (2021): 4294, https://doi.org/10.1038/s41467-021-24571-1.

14. X.-J. Kong and J.-R. Li, "An Overview of Metal–Organic Frameworks for Green Chemical Engineering," *Engineering* 7 (2021): 1115–1139.

15. Q. Dong, Y. Huang, J. Wan, et al., "Confining Water Nanotubes in a $Cu_{10}O_{13}$-Based Metal–Organic Framework for Propylene/Propane Separation with Record-High Selectivity," *Journal of the American Chemical Society* 145 (2023): 8043–8051, https://doi.org/10.1021/jacs.3c00515.

16. K. Zhou, Y. Zhou, Z. Jia, et al., "Single-Crystal Metal-Organic Frameworks for Electronic and Opto-Electronic Devices," *Cell Reports Physical Science* 4 (2023): 101656, https://doi.org/10.1016/j.xcrp.2023.101656.

17. A. Wang, M. Walden, R. Ettlinger, et al., "Biomedical Metal–Organic Framework Materials: Perspectives and Challenges," *Advanced Functional Materials* 34 (2024): 2308589, https://doi.org/10.1002/adfm.202308589.

18. I. Abánades Lázaro, X. Chen, M. Ding, et al., "Metal–organic Frameworks for Biological Applications," *Nature Reviews Methods Primers* 4 (2024): 42, https://doi.org/10.1038/s43586-024-00320-8.

19. J. Łuczak, M. Kroczewska, M. Baluk, J. Sowik, P. Mazierski, and A. Zaleska-Medynska, "Morphology control through the synthesis of metal-organic frameworks," *Advances in Colloid and Interface Science* 314 (2023): 102864.

20. G.-X. Liu, H. Xu, H. Zhou, S. Nishihara, and X.-M. Ren, "Temperature-Induced Assembly of MOF Polymorphs: Syntheses, Structures and Physical Properties," *CrystEngComm* 14 (2012): 1856, https://doi.org/10.1039/c1ce05369h.

21. Y.-X. Sun and W.-Y. Sun, "Influence of Temperature on Metal-Organic Frameworks," *Chinese Chemical Letters* 25 (2014): 823–828, https://doi.org/10.1016/j.cclet.2014.04.032.

22. N. Missaoui, A. Chrouda, F. Bourguiba, and J. Serafin, "Impact of Metal Precursor and Molar Ratios on Adsorption and Separation of CO_2 and CH_4 by SOD-ZIF-67 Prepared Using Green Solvent-Free Synthesis," *Fuel* 378 (2024): 132840, https://doi.org/10.1016/j.fuel.2024.132840.

23. S. Leubner, R. Stäglich, J. Franke, et al., "Solvent Impact on the Properties of Benchmark Metal–Organic Frameworks: Acetonitrile-Based Synthesis of CAU-10, Ce-UiO-66, and Al-MIL-53," *Chemistry – A European Journal* 26 (2020): 3877–3883.

24. B. Pramanik, R. Sahoo, and M. C. Das, "pH-Stable MOFs: Design Principles and Applications," *Coordination Chemistry Reviews* 493 (2023): 215301, https://doi.org/10.1016/j.ccr.2023.215301.

25. Y. Chen, C. Yang, X. Wang, J. Yang, K. Ouyang, and J. Li, "Kinetically Controlled Ammonia Vapor Diffusion Synthesis of a Zn(ii) MOF and Its H_2O/NH_3 Adsorption Properties," *Journal of Materials Chemistry A* 4 (2016): 10345–10351, https://doi.org/10.1039/C6TA03314H.

26. H. Li, M. Eddaoudi, M. O'Keeffe, and O. M. Yaghi, "Design and Synthesis of an Exceptionally Stable and Highly Porous Metal-Organic Framework," *Nature* 402 (1999): 276–279, https://doi.org/10.1038/46248.

27. K. M. Snook, L. B. Zasada, D. Chehada, and D. J. Xiao, "Oxidative Control over the Morphology of Cu_3(HHTP)$_2$, a 2D Conductive Metal–organic Framework," *Chemical Science* 13 (2022): 10472–10478, https://doi.org/10.1039/D2SC03648G.

28. S. Shen, P. Tan, Y. Tang, G. Duan, and Y. Luo, "Adjustable Synthesis of Ni-Based Metal–Organic Framework Membranes and Their Field-Effect Transistor Sensors for Mercury Detection," *ACS Applied Electronic Materials* 4 (2022): 622–630, https://doi.org/10.1021/acsaelm.1c01009.

29. F. Bigdeli, M. N. A. Fetzer, B. Nis, A. Morsali, and C. Janiak, "Coordination Modulation: A Way to Improve the Properties of Metal–Organic Frameworks," *Journal of Materials Chemistry A* 11 (2023): 22105–22131, https://doi.org/10.1039/D3TA03077F.

30. L. Li, L. Guan, A. Zhu, Y. An, S. Dong, and J.-J. Zhu, "Regulation of Triazine-COF and CoAl-LDH Substrates in Composites for High-Performance Neurofilament-Light Chains Electrochemical Immunosensors," *Sensors and Actuators B: Chemical* 411 (2024): 135715, https://doi.org/10.1016/j.snb.2024.135715.

31. M. R. Hajmohammadi, P. Alipour, and H. Parsa, "Microfluidic Effects on the Heat Transfer Enhancement and Optimal Design of Microchannels Heat Sinks," *International Journal of Heat and Mass Transfer* 126 (2018): 808–815, https://doi.org/10.1016/j.ijheatmasstransfer.2018.06.037.

32. N. Rohra, G. Gaikwad, P. Dandekar, and R. Jain, "Microfluidic Synthesis of a Bioactive Metal–Organic Framework for Glucose-Responsive Insulin Delivery," *ACS Applied Materials & Interfaces* 14 (2022): 8251–8265, https://doi.org/10.1021/acsami.1c22153.

33. T. Lee, J. Kim, C. Park, et al., "Large-Area Synthesis of Ultrathin, Flexible, and Transparent Conductive Metal–Organic Framework Thin Films via a Microfluidic-Based Solution Shearing Process," *Advanced Materials* 34 (2022): 2107696, https://doi.org/10.1002/adma.202107696.

34. P. Coliaie, R. R. Bhawnani, A. Prajapati, et al., "Patterned Microfluidic Devices for Rapid Screening of Metal–organic Frameworks Yield Insights into Polymorphism and Non-Monotonic Growth," *Lab on a Chip* 22 (2022): 211–224, https://doi.org/10.1039/D1LC01086G.

35. C. Hu, Y. Bai, M. Hou, et al., "Defect-Induced Activity Enhancement of Enzyme-Encapsulated Metal-Organic Frameworks Revealed in Microfluidic Gradient Mixing Synthesis," *Science Advances* 6 (2020): aax5785, https://doi.org/10.1126/sciadv.aax5785.

36. D. Sheberla, L. Sun, M. A. Blood-Forsythe, et al., "High Electrical Conductivity in Ni_3 (2,3,6,7,10,11-Hexaiminotriphenylene) 2 , a Semiconducting Metal–Organic Graphene Analogue," *Journal of the American Chemical Society* 136 (2014): 8859–8862, https://doi.org/10.1021/ja502765n.

37. X.-H. Liu, Y.-W. Yang, X.-M. Liu, et al., "Confined Synthesis of Oriented Two-Dimensional Ni_3 (hexaiminotriphenylene) 2 Films for Electrocatalytic Oxygen Evolution Reaction," *Langmuir* 36 (2020): 7528–7532, https://doi.org/10.1021/acs.langmuir.0c01128.

38. L. Sun, B. Liao, D. Sheberla, et al., "A Microporous and Naturally Nanostructured Thermoelectric Metal-Organic Framework with Ultralow Thermal Conductivity," *Joule* 1 (2017): 168–177, https://doi.org/10.1016/j.joule.2017.07.018.

39. F. Fu, C. Wang, Q. Wang, et al., "Highly Selective and Sharp Volcano-Type Synergistic Ni_2 Pt@ZIF-8-Catalyzed Hydrogen Evolution from Ammonia Borane Hydrolysis," *Journal of the American Chemical Society* 140 (2018): 10034–10042, https://doi.org/10.1021/jacs.8b06511.

40. X. Ma, Y. He, D. Zhang, et al., "Cobalt-Based MOF-Derived CoP/Hierarchical Porous Carbon (HPC) Composites as Robust Catalyst for Efficient Dehydrogenation of Ammonia-Borane," *ChemistrySelect* 5 (2020): 2190–2196, https://doi.org/10.1002/slct.201904481.

41. S. Guan, Z. Yuan, S. Zhao, et al., "Efficient Hydrogen Generation from Ammonia Borane Hydrolysis on a Tandem Ruthenium–Platinum–Titanium Catalyst," *Angewandte Chemie International Edition* 63 (2024): 202408193, https://doi.org/10.1002/anie.202408193.

42. M. Shingole, S. Banerjee, P. Ruz, S. Kolay, A. Kumar, and V. Sudarsan, "Catalytic Hydrogen Generation through Ammonia Borane Hydrolysis Using Metal–Organic Framework via O–H Bond Activation," *Energy*

& Fuels 38 (2024): 8968–8978, https://doi.org/10.1021/acs.energyfuels.4c00529.

43. H. Zhao, W. Zhang, C. Liao, et al., "Efficient Hydrolytic Dehydrogenation of Ammonia Borane Catalyzed by Ultrafine Pt Clusters Confined in Ni–Ti Layered Double Hydroxides with Closo-Dodecaborate," *International Journal of Hydrogen Energy* 82 (2024): 901–909, https://doi.org/10.1016/j.ijhydene.2024.08.007.

44. S. Akbayrak and S. Özkar, "Nickel Ferrite Platinum Nanoparticles: Highly Active Catalyst in Hydrolytic Dehydrogenation of Ammonia Borane," *Journal of Alloys and Compounds* 1018 (2025): 179220, https://doi.org/10.1016/j.jallcom.2025.179220.

45. M. E. Foster, K. Sohlberg, M. D. Allendorf, and A. A. Talin, "Unraveling the Semiconducting/Metallic Discrepancy in Ni_3 (HITP) 2," *The Journal of Physical Chemistry Letters* 9 (2018): 481–486, https://doi.org/10.1021/acs.jpclett.7b03140.

46. R. W. Day, D. K. Bediako, M. Rezaee, et al., "Single Crystals of Electrically Conductive Two-Dimensional Metal–Organic Frameworks: Structural and Electrical Transport Properties," *ACS Central Science* 5: 1959–1964.

Supporting Information

Additional supporting information can be found online in the Supporting Information section.

Supporting File: smtd70746-sup-0001-SuppMat.docx.

Supporting Video: smtd70746-sup-0002-VideoS1.mp4.

Supporting Video: smtd70746-sup-0003-VideoS2.mp4.

Supporting Video: smtd70746-sup-0004-VideoS3.mp4.

Supporting Video: smtd70746-sup-0005-VideoS4.mp4.